A 3-kW Wireless Power Transfer System for Sightseeing Car Supercapacitor Charge

Zhenjie Li, Chunbo Zhu, *Member, IEEE*, Jinhai Jiang, Kai Song, *Member, IEEE*, and Guo Wei

***Abstract*—Wireless power transfer (WPT) is the preferred charging method for electric vehicles (EVs) powered by battery and supercapacitor. In this paper, a novel WPT system with constant current charging capability for sightseeing car with supercapacitor storage is designed. First, an optimized magnetic coupler using ferrite cores and magnetic shielding structure is proposed to ensure stable power transfer and high efficiency. Compared with the traditional planar shape ferrite core coupler, the proposed magnetic coupler requires lesser ferrite material without degrading the performance of the WPT system. Second, the model of supercapacitor is applied to the WPT system and the relationship between equivalent load resistances of supercapacitor and charging time is analyzed in detail. Then, a Buck converter with proportional integral (PI) controller is implemented on the secondary side to maintain constant charging current for the variable load. Finally, the proposed design is verified by experiments. Constant charging current of 31.5 A across transfer distance of 15 cm is achieved. The peak transfer power and system efficiency are 2.86 kW and 88.05%, respectively.**

***Index Terms*—Charging current regulation, magnetic coupler, supercapacitor (SC), variable load, wireless power transfer (WPT).**

I. Introduction

WIRELESS power transfer systems are gaining considerable attention for pure and plug-in hybrid electric vehicles (EVs) [1]–[5]. They have demonstrated many advantages including the conveniences of being cordless making it unnecessary to plug and unplug the bored wire, insusceptible to weather influence since the primary side is embedded underground for EVs charging applications, and so on. Despite those advantages, there are still some key issues to be addressed in the practical design of the WPT system. For example, EVs are always powered by battery, supercapacitor, or those two combined. The equivalent resistance of those power suppliers' changes dynamically during the charging process, and then the charging current and system efficiency will be affected inevitably [6], [7]. Therefore, it is essential to pay attention to the WPT system with a variable load. The constant charging current is always essential to shorten the charging time, especially when the fast charge for EVs is required. Compared with battery, supercapacitor, which is characterized by high power density, short charging time, and long life duration, is chosen as the power supply for the fast wireless charging EVs and used to research the WPT system with variable load in this paper.

In terms of the WPT system for supercapacitor charge, a number of publications mainly focus on the analysis of power control, charging circuit design, and so on [8]–[12]. In [8] and [9], dc–dc converters are proposed to control the power flow and the control schemes are also analyzed. In [10] and [11], the WPT systems for supercapacitor powered implantable devices are proposed, and circuits are designed and experimented to meet the size requirements. However, all these publications did not provide an overall system design process and analyze the model of supercapacitor that can be applied to the WPT system, especially for high transferred power condition. In [13]–[16], several different types of supercapacitor models are analyzed and the classical circuit model is proposed. It shows that the equivalent resistance of supercapacitor changes dynamically with charging time [6], [16]. However, the equations between equivalent resistance and charging time are not deduced in-depth. Based on the analysis of supercapacitor model in the WPT system, the main motivation of this paper is to fulfill the whole system modeling, overall design and constant charging current control.

In general, with the consideration of different load and tire pressure conditions, the normal distance between the EVs' chassis and ground is always in the range of 15–25 cm. The magnetic coupler's coupling coefficient is relatively low, for the reason that leakage magnetic flux is high through the long transfer distance between the primary and secondary sides [1], [4]. Hence, the magnetic coupler should be properly designed to ensure stable power transfer and high efficiency, especially for the WPT system with a variable load. The commonly used structures of magnetic coupler in stationary EVs wireless charging are circular and rectangular type, because they have simple and compact structures as well as low electromagnetic field (EMF) for pedestrians [17]–[20]. In [17], it is proved that the larger the area of magnetic coupler is, the larger the mutual inductance is. Meanwhile, assume the rectangle's length and width are the same as the diameter of circle, then the area of rectangle is larger than circle by the ratio of 1.27. It means that the rectangular type magnetic has a larger mutual inductance than circular type. In [18], the magnetic coupler of circular type is optimized from

Manuscript received December 4, 2015; revised May 15, 2016; accepted June 17, 2016. Date of publication June 24, 2016; date of current version February 2, 2017. This work was supported by the National Natural Science Foundation of China under Grants 51577034 and 51577041. Recommended for publication by Associate Editor O. C. Onar.

The authors are with the School of Electrical Engineering & Automation, Harbin Institute of Technology, Harbin 150001, China (e-mail: lizhenjie0725@163.com; kaisong@hit.edu.cn; wg_weiguo@sina.com; 306658940@qq.com zhuchunbo@hit.edu.cn).

This paper has supplementary downloadable multimedia material available at http://ieeexplore.ieee.org provided by the authors. This material is 31 MB in size.

Color versions of one or more of the figures in this paper are available online at http://ieeexplore.ieee.org.

Digital Object Identifier 10.1109/TPEL.2016.2584701

coil width, ferrite cores, and so on. With the designed 700-mm diameter coupler, the 2-kW power has been transferred under a 200-mm air gap. In [19], the bipolar single-sided flux magnetic coupler of rectangular type (DD pad) with a size of 800 mm* 540 mm achieves 2-kW power transfer and provides a charge zone much larger than the circular pad. In practical applications, for the above two type magnetic couplers, they will face two problems: the magnetic coupler is too large to install on the EVs' chassis and the magnetic field may not meet the safety requirements by the International Commission on Non-ionizing Radiation Protection (ICNIRP) guidelines [21]. In this paper, in order to avoid the above problems, a much smaller magnetic coupler with the size of 400 mm $*$ 400 mm and optimized ferrite cores and magnetic shielding structure is well designed.

Once the structure of magnetic coupler is determined, the magnetic materials such as ferrite cores could be used to enhance coupling coefficient and magnetic shielding. In [21] and [22], MnZn material ferrite cores are selected as core material for using in the WPT system, because they exhibit high magnetic flux saturation and low loss when operates below 100 kHz. However, due to the limited magnetic shielding capability of ferrite cores, the Aluminum (Al) sheet is proposed to further suppress the magnetic field, and then the eddy current loss in the EVs' chassis is further reduced [23], [24]. Beyond the optimized magnetic coupler, control schemes are also essential to realize the constant current charging for supercapacitor. There are mainly three types of closed-loop control schemes, which can be classified as frequency tracking, impedance matching, and dc–dc conversion [6].

1) The constant charging current against load variations can be achieved by tracking the spilt frequencies in the "over coupled" region if the coupled resonances are lossless [25], [26].
2) In [27] and [28], the dynamic impedance matching circuits controlled by switches are proposed. Those methods allow the system to operate at a fixed frequency and regulate the charging current or voltage.
3) The usage of dc–dc converter on the primary or secondary side is also an effective way to adjust the charging current or voltage [29], [30].

Among those control schemes, frequency tracking may result in power transfer capability decreases if the frequency shifts too large from the optimal point, and then cause the system instability due to the occurrence of bifurcation with variable load. The dynamic impedance matching scheme is always used under high frequency and low power condition. Meanwhile, this scheme needs an array of capacitors, which may add additional weight, size, and control complexity of the system. The dc–dc conversion can minimize the effect of variable load on the system through impedance adjustment, which means the WPT system can work at fixed frequency mode and alleviate the need of a tunable impedance matching network. In addition, the closed-loop control schemes can also be classified as primary side control [1], secondary side control [31], and dual side control [32]. Compared with the primary and dual side control, secondary side control avoids the power flow communication between the primary and secondary sides, and then the control speed and stability of transferred power are ensured. Hence, Buck converter with secondary side control is designed to achieve the goal of charging current regulation in this paper.

Based on the given analysis, a novel design of magnetic coupler based on patent [33] and control scheme of constant current charging regulation for WPT system with variable load are discussed. The goals of lower weight, cost, EMF, and smaller size for the proposed magnetic coupler are achieved. In addition, the variable load characteristic of supercapacitor is analyzed by circuit modeling, and Buck converter with closed-loop control scheme is implemented to regulate the charging current under the variable load condition. The rest sections of this paper are organized as follows: Section II analyzes the system structure and circuit model. Section III optimizes the ferrite cores and magnetic shielding structure of the proposed magnetic coupler. Section IV analyzes the model of supercapacitor and control scheme of Buck converter. Section V validates the designed WPT system with experiments. Finally, the conclusion is shown in Section VI.

II. System Structure and Theoretical Analysis

A. System Structure

In most applications, the WPT system is fed by an ac voltage source, and then provides dc voltage to the load. It is mainly composed of two electrically isolated parts named as primary side and secondary side, as shown in Fig. 1. For the dc–ac stage on the primary side, there are mainly two types of H-bridge inverter, the voltage source inverter (VSI) and current source inverter (CSI) [34]. The advantages of CSI topology are inherent short-circuit protection, long lifetime of the inductor, and reduced current stress; however, the inductor is always costly and high voltage stress occurs on the switches. Compared with CSI topology, the VSI topology, which is much more common in power electronics inverters presently, do not require bulky inductor and only use electrolytic capacitors to provide constant voltage [35], [36]. When combining with resonance or compensation topologies in the WPT system, the advantages of VSI topology are even more prominent.

As mentioned in [37], among the four basic compensation topologies, only the reactance of series–series (SS) topology looking from the primary side is independent of either the coupling coefficient or load at secondary side resonant frequency. Furthermore, the power reflection from secondary side to primary side is eliminated at this frequency. In [32] and [38], the SS topology is proposed for the WPT system with wide load range, and has the current source behavior on the secondary side when the primary side operates as a voltage source inverter, which makes it a good candidate for battery and supercapacitor charge.

And then the SS topology combined with VSI topology is selected for this system. In addition, the system operating frequency is chosen as 85.5 kHz, which is aimed to satisfy the standard J2954 (nominal frequency range is 81.38–90.00 kHz for light-duty passenger electric vehicle) drafted by the Society of Automotive Engineers task force [39].

On the primary side, the rectifier stage converts the single phase 50-Hz ac voltage to dc voltage, then the VSI topology H-bridge inverter outputs high frequency ac current to the primary side coil, and then establishes the high frequency magnetic field.

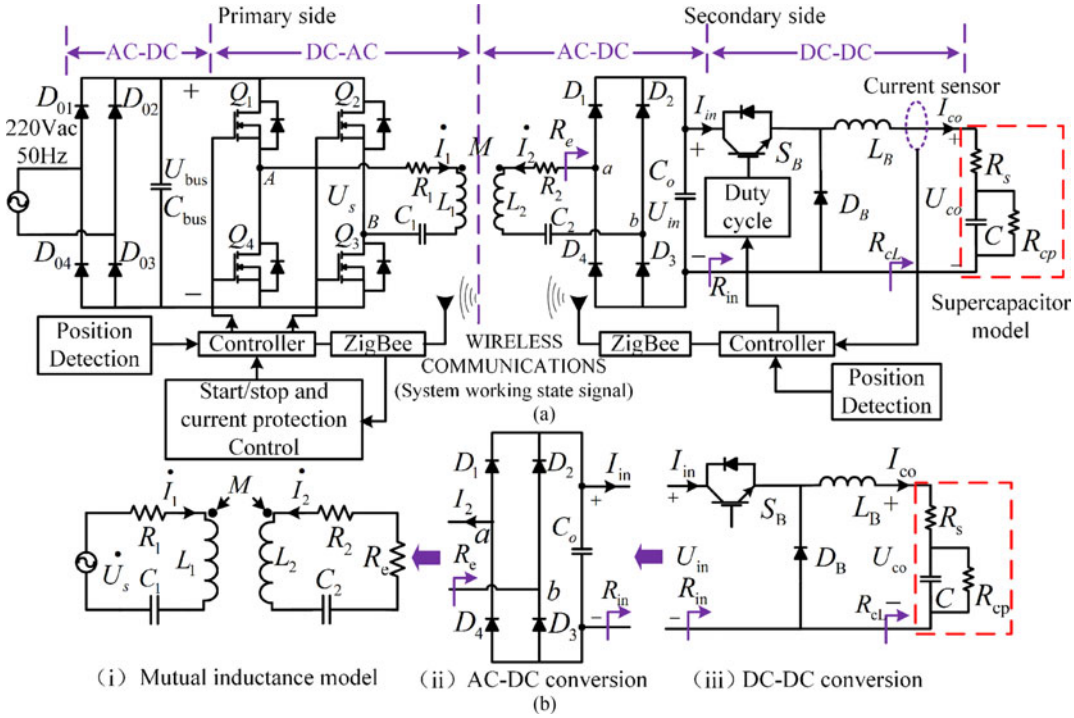

Fig. 1. WPT system structure diagram and circuit model. (a) Whole system structure and (b) equivalent circuit model.

The high frequency voltage is transferred to the secondary side coil through magnetic coupling, and then the secondary side rectifier stage converts the ac voltage to dc voltage. Finally, the secondary side Buck converter regulates this dc voltage to charge supercapacitor with constant current. The controller on the primary side is mainly used to monitor system working state via wireless communications between the primary and secondary sides, such as the signal of car detecting or positioning, start or stop charging, over current protection and so on. Optionally, the position detection devices could be installed to guide the drivers to achieve an accurate parking position [40], [41], and the method for car positioning and detecting in this system is described in Section V-A.

B. Circuit Modeling

As shown in Fig. 1(a), Q_1-Q_4 are four power metallic oxide semiconductor field effect transistors (MOSFETs) that constitute the H-bridge inverter on primary side. $L_{\rm i}, R_{\rm i}, C_{\rm i}$, and $I_i (i = 1, 2)$ are the coils self-inductance, resistance, corresponding resonant capacitors and resonant current of primary or secondary side. M is the mutual inductance between two coils. D_1-D_4 are the secondary side rectifier diodes. $S_{\rm B}, D_{\rm B}$, $L_{\rm B}$, and $C_{\rm B}$ constitute the Buck converter. $R_{\rm s}, C$, and $R_{\rm cp}$ model the equivalent circuit of the supercapacitor. $U_{\rm s}$ and $U_{\rm bus}$ are the equivalent output ac voltage and input dc voltage of H-bridge inverter. $R_{\rm e}$, $R_{\rm in}$, and $I_{\rm in}$ are the equivalent resistance, output resistance, and output current of the secondary side rectifier. $R_{\rm cL}$ is the equivalent load resistance of the supercapacitor, which will be analyzed in Section IV.

In general, the resonant currents are almost sine waves because of high quality factors of the resonant tanks in WPT system. Fundamental harmonic analysis based on the circuit model has sufficient accuracy for the steady-state analysis of WPT system [6]. As shown in Fig. 1(b)-(ii), in terms of series resonant secondary side with a capacitive output filter, the rectifier is driven with a current source and a square wave of voltage appears at the input of the rectifier [42], [43]. Then, the equations of $R_{\rm e}$ and $I_{\rm in}$ of the secondary side rectifier are given by

$$R_{\rm e} = \frac{8}{\pi^2} R_{\rm in} \tag{1}$$

$$I_{\rm in} = \frac{2\sqrt{2}}{\pi} I_2. \tag{2}$$

According to Kirchhoff's voltage law (KVL), the WPT system can be described by the following equations:

$$\begin{cases} \left(R_1 + j\omega L_1 + \dfrac{1}{j\omega C_1}\right) \cdot \dot{I}_1 + j\omega M \cdot \dot{I}_2 = \dot{U}_s \\ j\omega M \cdot \dot{I}_1 + \left(R_2 + R_{\rm e} + j\omega L_2 + \dfrac{1}{j\omega C_2}\right) \cdot \dot{I}_2 = 0 \end{cases} \tag{3}$$

where $\dot{U}_s$, $\dot{I}_1$, and $\dot{I}_2$ are the phasors of fundamental harmonics of the equivalent output ac voltage, primary side resonant current, and secondary side resonant current; U_s, I_1, and I_2 are the corresponding root-mean-square (RMS) values, respectively; ω stands for the angular operating frequency and *j* is the imaginary unit. Through the Fourier decomposition of the square wave that generated by the H-bridge inverter, U_s is expressed as

$$U_s = \left\| \dot{U}_s \right\| = \frac{2\sqrt{2}}{\pi} U_{\rm bus}. \tag{4}$$

Then, resonant currents $\dot{I}_1$ and $\dot{I}_2$ are deduced by the following equations:

$$\begin{cases} \dot{I}_1 = \frac{Z_2 Z_4}{Z_1 Z_2 - Z_3} \dot{U}_s \\ \dot{I}_2 = j \frac{Z_3}{Z_1 Z_2 - Z_3} \dot{U}_s \end{cases} \tag{5}$$

$$\begin{cases} Z_1 = j\omega C_1 R_1 + (1 - \omega L_1 C_1) \\ Z_2 = j\omega C_2 (R_2 + R_e) + (1 - \omega L_2 C_2) \\ Z_3 = \omega^2 C_1 C_2 (\omega M)^2 \\ Z_4 = j\omega C_1 \end{cases}. \tag{6}$$

If the WPT system's angular operating frequency equals or approximately equals to the resonant frequency of secondary and primary side, we have

$$\omega = \sqrt{\frac{1}{C_2 L_2}} \approx \sqrt{\frac{1}{C_1 L_1}}. \tag{7}$$

The terms $\omega^2 C_2 L_2$ and $\omega^2 C_1 L_1$ will be equal or very close to one, and then (5) is further simplified as

$$\begin{cases} \dot{I}_1 = \dfrac{R_2 + R_e}{R_1 (R_2 + R_e) + (\omega M)^2} \dot{U}_s \\ \dot{I}_2 = \dfrac{1}{j} \dfrac{\omega M}{R_1 (R_2 + R_e) + (\omega M)^2} \dot{U}_s \end{cases}. \tag{8}$$

Therefore, the RMS values of resonant current I_1 and I_2 are

$$\begin{cases} I_1 = \dfrac{R_2 + R_e}{R_1 (R_2 + R_e) + (\omega M)^2} \dfrac{2\sqrt{2}}{\pi} U_{\text{bus}} \\ I_2 = \dfrac{\omega M}{R_1 (R_2 + R_e) + (\omega M)^2} \dfrac{2\sqrt{2}}{\pi} U_{\text{bus}} \end{cases}. \tag{9}$$

Further, combined with (2) and (9), the input current of the Buck converter I_{in}, which is also the output current of the secondary side rectifier, is determined as follows:

$$I_{\text{in}} = \frac{\omega M}{R_1 (R_2 + R_e) + (\omega M)^2} \frac{8}{\pi^2} U_{\text{bus}}. \tag{10}$$

The expression of the system output power can be obtained by

$$P_{\text{co}} = I_2^2 R_e = \frac{(\omega M)^2 R_e}{\left[R_1 (R_2 + R_e) + (\omega M)^2\right]^2} \frac{8}{\pi^2} U_{\text{bus}}^2. \tag{11}$$

Here, R_e depends on R_{in} as shown in (1). In the following Section II-C, it shows that R_{in} depends on equivalent load resistance R_{cL} and Buck converter's duty cycle D, which means R_e is a function of R_{cL} and D.

The system efficiency, taking the primary and secondary side coils' losses into consideration, is

$$\eta = \frac{P_{\text{co}}}{P_{\text{in}}} = \frac{I_2^2 R_e}{I_1^2 R_1 + I_2^2 R_2 + I_2^2 R_e} = \frac{(\omega M)^2 \cdot R_e}{(R_2 + R_e)\left[R_1 (R_2 + R_e) + (\omega M)^2\right]}. \tag{12}$$

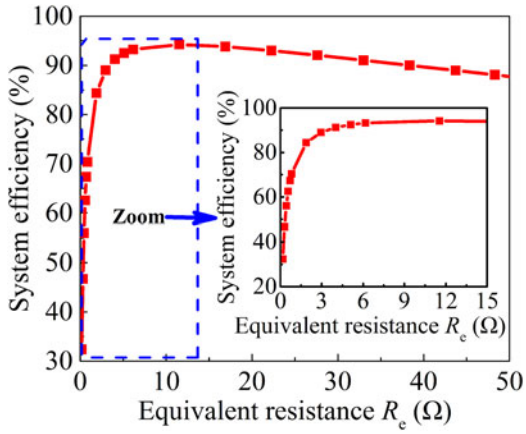

Fig. 2. System efficiency versus the equivalent resistance of the secondary side rectifier.

The system efficiency is defined as the ratio of system output power P_{co} to input power P_{in}, and the changes of R_e and M will influence the system efficiency. When the efficiencies of the H-bridge inverter, magnetic coupler, secondary side rectifier, and Buck converter are considered, actual system efficiency η_{loss} could be calculated by multiplying their own efficiency ratios to (12), respectively.

Through the derivation of η, $R_{e\max}$ that ensures the maximum system efficiency is expressed as

$$R_{e\max} = \sqrt{\frac{R_2}{R_1}\left[R_1 R_2 + (\omega M)^2\right]}. \tag{13}$$

According to (12) and (13), it is obvious that the system efficiency increases with the equivalent resistance firstly, and then decreases, as shown in Fig. 2. In addition, $R_{e\max}$ mainly depends on the mutual inductance, which is a constant value once the magnetic coupler and transfer distance are determined.

C. DC–DC Converter Modeling

Generally, in order to track the maximum system efficiency point, dc–dc converters on the secondary side are used, especially for the WPT system with variable and wide load range [6], [44]. In addition, dc–dc converters can be also applied to adjust the charging current or voltage, as mentioned in Section I. In [45], it is shown that with the closed-loop control of the duty cycle, the input resistance of dc–dc converter can be adjusted accordingly, and then the constant charging current is achieved. The characteristics of four common dc–dc converters in terms of their input resistance adjustment capability are summarized in Table I, where D, U_{in}, and U_{out} are the duty cycle, input and output voltages, respectively.

As shown in Table I, the Cuk converter has the opposite polarity between its input and output. The Buck–Boost converter may add additional power losses to the WPT system, especially under several kilowatt levels or higher power transfer condition. The Boost converter can only adjust the input resistance with a limited range of $0-R_{\text{L}}$. On this basis, the Buck converter is proposed in this system. Through the adjustment of Buck

TABLE I
COMPARISON OF BASIC DC–DC CONVERTERS

Topology	Output voltage U_{out}	Input resistance R_{in}	Input resistance range
Buck	DU_{in}	R_L/D^2	R_L to $+\infty$
Boost	$\frac{U_{in}}{(1-D)}$	$(1-D)^2 R_L$	0 to R_L
Buck–Boost	$\frac{DU_{in}}{(1-D)}$	$\frac{(1-D)^2 R_L}{D^2}$	0 to $+\infty$
Cuk	$\frac{-DU_{in}}{(1-D)}$	$\frac{(1-D)^2 R_L}{D^2}$	0 to $+\infty$

converter's duty cycle with closed-loop control scheme, its input resistance can be adjusted dynamically, so as to regulate the charging current [9].

As shown in Fig. 1(b)-(iii), suppose that the power losses in the Buck converter are small and can be ignored for the convenience of analysis [6], [7], the relationships between the input and output voltages are

$$\frac{U_{\rm in}^2}{R_{\rm in}} = \frac{U_{\rm co}^2}{R_{\rm cL}} \tag{14}$$

$$U_{\rm in} = \frac{1}{D} U_{co} \tag{15}$$

where $U_{\rm in}$ and $U_{\rm co}$ are the input and output voltages, respectively; $R_{\rm in}$ and D are the input resistance and duty cycle of the Buck converter, respectively; $R_{\rm cL}$ is a time related value, which will be analyzed in Section IV-A. By using (14) and (15), the following equations are obtained:

$$R_{\rm in} = \frac{1}{D^2} R_{\rm cL} \tag{16}$$

$$I_{\rm co} = \frac{1}{D} I_{\rm in}. \tag{17}$$

Then, combined with (1), (10), (16), and (17), the charging current and system efficiency are expressed as

$$I_{\rm co} = \frac{8D(\omega M) U_{\rm bus}}{R_1 \left[R_2 (\pi D)^2 + 8R_{\rm cL}\right] + (\omega M)^2 (\pi D)^2} \tag{18}$$

$$\eta = \frac{8(\omega M)^2 (\pi D)^2 R_{\rm cL}}{R_1 \left[R_2 (\pi D)^2 + 8R_{\rm cL}\right]^2 + (\omega M)^2 (\pi D)^2 \left[R_2 (\pi D)^2 + 8R_{\rm cL}\right]}. \tag{19}$$

The charging current $I_{\rm co}$ and system efficiency η as a function of equivalent load resistance $R_{\rm cL}$ and duty cycle D are analyzed by Pspice circuit simulation software, and then the results are plotted in Fig. 3. When the range of $R_{\rm cL}$ is $0.3-3\,\Omega$, with the increment of $R_{\rm cL}$, the system efficiency increases which is consistent with Fig. 2, and the charging current decreases. For a fixed $R_{\rm cL}$, the larger the duty cycle is, the smaller the system efficiency and charging current are. With the duty cycle increases per 0.1, the charging current decreases 3–7 A. Once

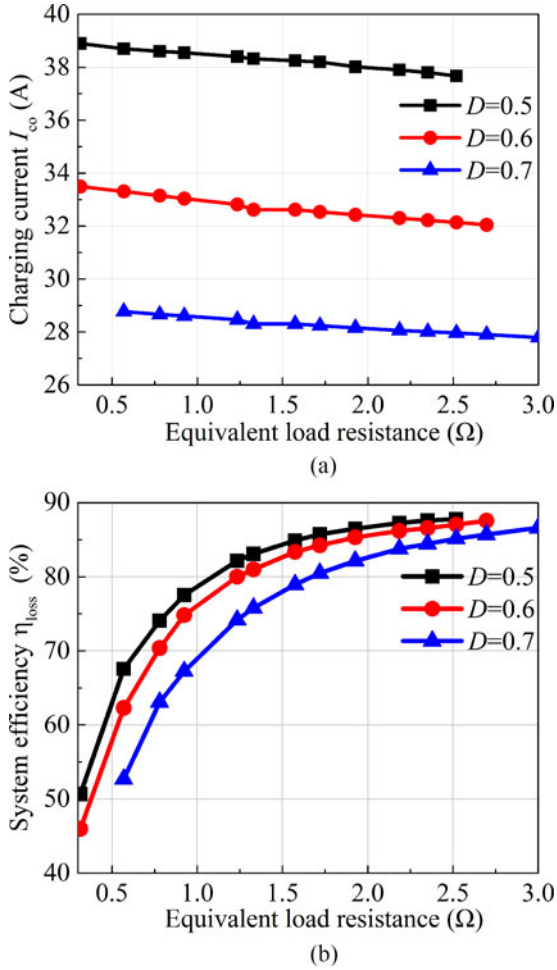

Fig. 3. Curves of the duty cycle and equivalent load resistance with (a) charging current and (b) system efficiency.

the magnetic coupler is fabricated, mutual inductance is almost fixed unless misalignment occurs. Hence, the adjustment of duty cycle can be used to regulate the charging current.

In addition, in order to obtain the suitable mutual inductance for the magnetic coupler that will be designed in Section III, mutual inductance $M_{\rm max}$ for the maximum charging current $I_{\rm comax}$ is analyzed and expressed as

$$I_{\rm comax} = \frac{4U_{\rm bus}}{\pi} \frac{1}{\sqrt{R_1 \left[R_2 (\pi D)^2 + 8R_{\rm cL}\right]}} \tag{20}$$

$$M_{\rm max} = \frac{\sqrt{R_1 \left[R_2 (\pi D)^2 + 8R_{\rm cL}\right]}}{\omega (\pi D)}. \tag{21}$$

It is obvious that the charging current increases with mutual inductance first, and then decreases, as shown in Fig. 4. With the increase of $R_{\rm cL}$, mutual inductance $M_{\rm max}$ for the maximum charging current increases. When $R_{\rm cL}$ is small, the change trend of charging current versus mutual inductance is obvious. With the increase of D, mutual inductance $M_{\rm max}$ for the maximum charging current decreases. When the range of $R_{\rm cL}$ is $0.3-3\,\Omega$

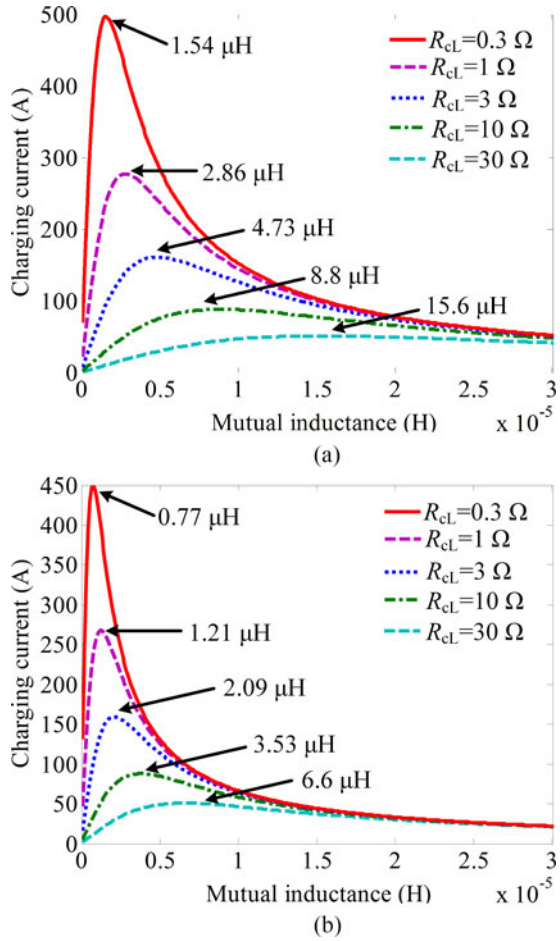

Fig. 4. Curves of the mutual inductance and equivalent load resistance versus charging current. (a) $D = 0.3$ and (b) $D = 0.7$.

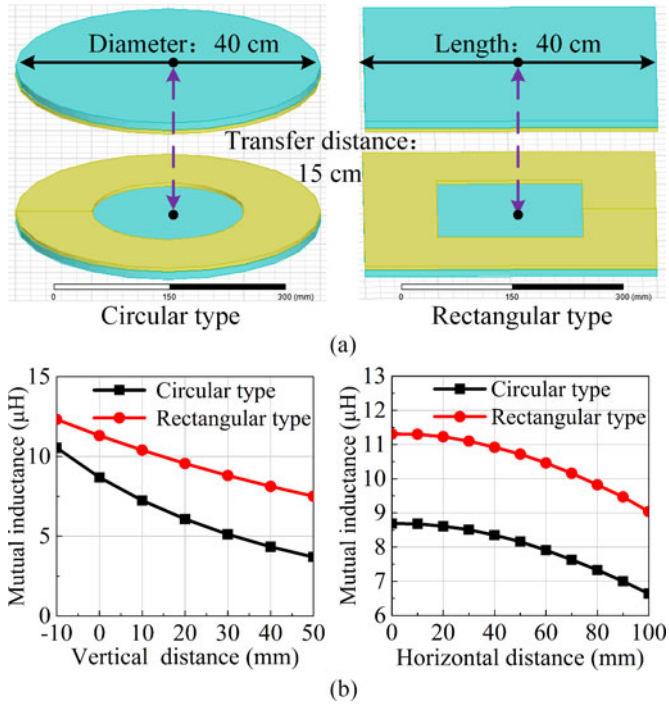

Fig. 5. Comparison between circular and rectangular type magnetic couplers. (a) Simulation model and (b) vertical and horizontal misalignment.

and *D* is 0.3 and 0.7, the calculated $M_{\max}$ is much smaller than $5\,\mu$H.

III. Magnetic Coupler Design for the WPT System

Once the rectangular type magnetic coupler is selected for the WPT system, the finite element analysis (FEA) software (Ansoft Maxwell) based optimizations are undertaken prior to fabricate it. The main goals of FEA optimization should meet the following requirements [4], [5], [20]:

1) achieving the reasonable mutual inductance, which can ensure the stable power transfer and high efficiency;
2) reducing the physical weight, size, and material cost as much as possible without sacrificing the power transfer capabilities, which is essential for the practical applications;
3) avoiding the magnetic saturation occurs under the maximum transfer power, especially when the transferred power is high;
4) meeting the magnetic field safety requirements regulated by ICNIRP guidelines.

The optimization process of the magnetic coupler can be described as following. First, in order to reduce weight and cost, the structure of ferrite core is optimized. Second, the magnetic field around the receiver is significantly reduced by the usage of Al sheet. The misalignment capability of magnetic coupler is also analyzed to properly design the system power electronics and closed-loop control scheme.

A. Mutual Inductance Optimization

The mutual inductance, which is significantly affected by the design of the magnetic coupler, is always considered as an important factor in the WPT system. Hence, the rationality of selecting the rectangular type magnetic coupler is validated by Ansoft Maxwell simulation firstly, as shown in Fig. 5.

From Fig. 5, it can be seen that when the magnetic couplers' size (rectangle's length and width equal to circle's diameter) and the misalignment distance are same, the mutual inductance of rectangular type is much larger than circular type, and then the rectangular type is chosen. Furthermore, the mutual inductance determines the system power transfer capability, such as system output power, charging current, and system efficiency. Therefore, the mutual inductance versus charging current is simulated and the results are plotted in Fig. 6.

As shown in Fig. 6, the mutual inductance *M* should be chosen in the range of $22 - 24\,\mu$H, so as to meet the required 31.5-A charging current. In addition, due to *M* is always larger than the $M_{\max}$ (its value is smaller than $5\,\mu$H, as shown in Fig. 4) that achieves the maximum charging current, with the increase of mutual inductance, the charging current decreases. Also, the charging current decreases with the increase of the equivalent load resistance.

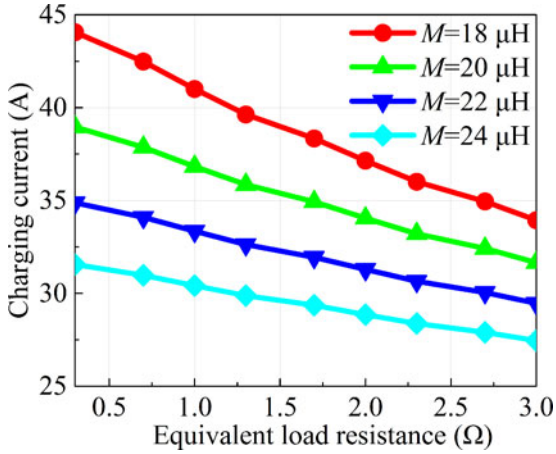

Fig. 6. Mutual inductance versus charging current.

B. Ferrite Core Optimization for the Magnetic Coupler

Once the required mutual inductance is determined, the optimal design of a magnetic coupler should always be considered. In [46], it points out that with the similar geometry and materials, different configurations of the magnetic coupler have different mutual inductances, and a better design may lead to a 50–100% improvement compared with the nonoptimal design. Hence, the magnetic coupler is optimized from the ferrite core and magnetic shielding.

In general, the ferrite core is applied to enhance the mutual inductance and magnetic shielding for the magnetic coupler, especially under large air gap situation. As shown in Fig. 7, the magnetic couplers with and without ferrite core (named as Type I and Type II) are simulated by Ansoft Maxwell. From the magnetic field simulation, it is obvious that the magnetic field around the receiver of Type II coupler is significantly suppressed by the ferrite core when compared with Type I coupler. Meanwhile, according to the simulation results in Fig. 8, with the usage of ferrite core, mutual inductance can be twice improved at least.

Based on the consideration that the receiver is mounted under the EV chassis, its weight and size should be small as possible, so as to adapt to the limited space. Combined with the required mutual inductance's range of the Type II magnetic coupler, $N_1 = 14$ and $N_2 = 8$ whose mutual inductance is $23.4\ \mu$H is suitable. In addition, the weight and cost of the magnetic coupler should be further reduced without sacrificing system performance, which is essential to the practical applications.

One intuitive way is to reduce the usage of ferrite core that always occupies a large part of weigh and cost in the magnetic coupler. Hence, Type III and IV couplers, which have the same coil turns as Type II coupler, are proposed, as shown in Fig. 7.

According to Table II, it is obvious that Type III coupler is not suitable for the reason that its mutual inductance fail to meet the required value, even though the usage of ferrite core is the least. Type II and IV couplers almost have the same mutual inductance and magnetic shielding effect, but the usage of ferrite core in type IV coupler is 31.25% less than type II coupler. Therefore, Type IV coupler is chosen in this paper. In addition, as shown in Fig. 7, the maximum magnetic flux in and around the Type IV coupler is less than $240\ \mu$T, which is much smaller than the saturation magnetic flux. However, in order to design a stable WPT system, the saturation should always be considered, especially when the system output power is high, such as several tens or hundreds kilowatt level.

C. Magnetic Shielding Optimization for the Proposed Magnetic Coupler

Even though the ferrite core can suppress the magnetic field above the receiver to some extent, the magnetic shielding should be further considered. Because when the magnetic flux enters the chassis, it may cause eddy current losses and impact the electronic equipment in the EVs. As shown in Fig. 9, with the optimized Aluminum sheet, the magnetic field above the receiver is largely reduced and the eddy current mainly concentrates on the Aluminum sheet above the coils in the magnetic coupler. However, as the eddy current on the Aluminum sheet cancels the magnetic field, the mutual inductance decreases to $18.23\ \mu$H.

As mentioned before, the mutual inductance should be chosen in the range of $22 - 24\ \mu$H. Without changing the optimized structure of the ferrite core, coil turns should be redesigned, and then $N_1 = 15$ and $N_2 = 9$ with the mutual inductance (simulation result) of $22.4\ \mu$H is chosen. Combined with the skin depth due to eddy current, the thickness of the Aluminum sheet is chosen to be 2 mm.

D. Misalignment of Vertical and Horizontal

Considering the actual wireless charging situation, when the car is overload or parking misalignment occurs, mutual inductance will change, and then system power transfer capability will be influenced inevitably. Both the simulations by Ansoft Maxwell and experiments by Agilent Precision Impedance Analyzer E4990A are done to analyze the misalignment's influence on the mutual inductance and charging current, and the results are plotted in Fig. 10. It shows that the larger the vertical and horizontal misalignment distances are, the smaller the mutual inductance is. Meanwhile, when the misalignment increases, the charging current increases accordingly. In particular, Fig. 10 also proves that the simulation results of the mutual inductance are very consistent with the experiment results, and the error is less than 3%.

IV. Supercapacitor Model and Secondary Control

A. Equivalent Circuit Model of Supercapacitor

To design the supercapacitor powered WPT system, it is essential to have a model that describes the electric behavior of the supercapacitor load. In general, basic circuit components such as resistor and capacitor are used to model the supercapacitor. For researchers in the electric engineering field, the most widely used supercapacitor model is the classical equivalent circuit model [15], as shown in Fig. 11.

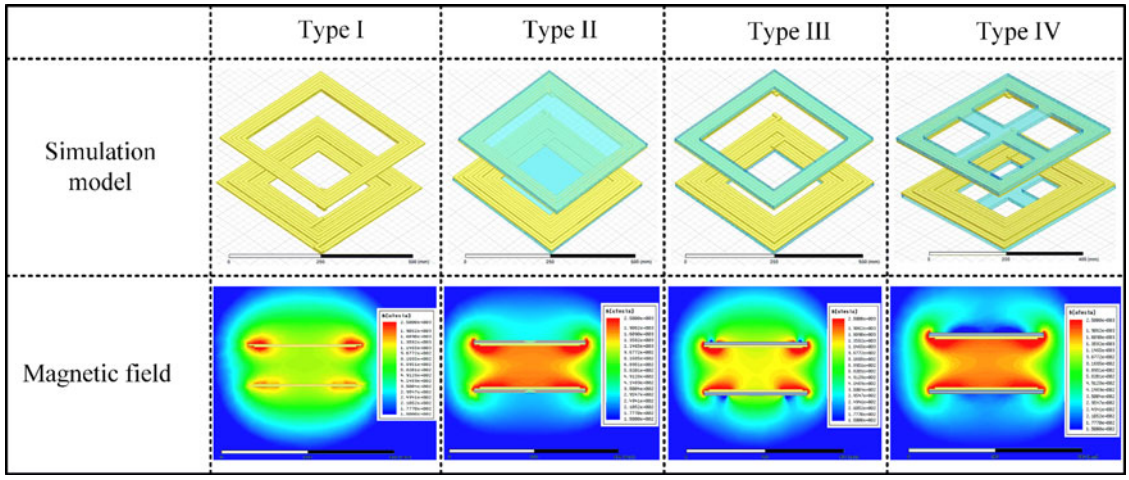

Fig. 7. Different types of magnetic couplers. (Color in the simulation model. yellow: coil, light blue: ferrite cores, and the range of magnetic flux is $150-2500\ \mu\mathrm{T}$. The applied primary and secondary side currents for simulation and experimental are 11 and 19 A.)

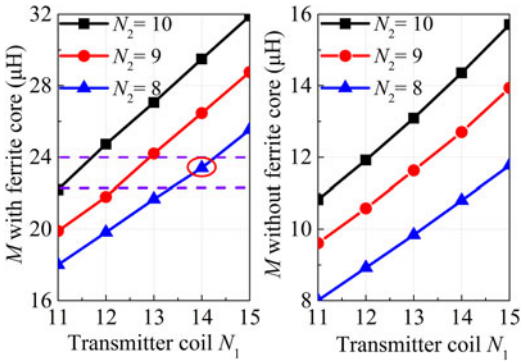

Fig. 8. Mutual inductance M versus coil turns.

TABLE II
PARAMETERS OF THREE TYPES MAGNETIC COUPLERS

Type	Mutual inductance (μH)	Ferrite cores usage (pieces)
II	23.4	32
III	18.1	18
IV	22.8	22

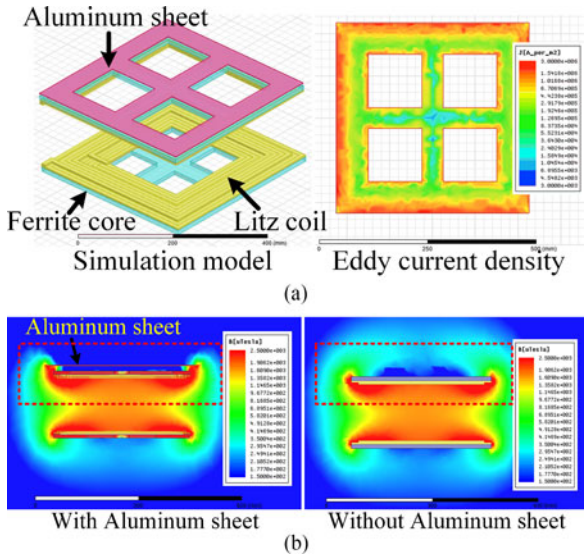

Fig. 9. Magnetic shielding simulation. (a) Simulation model and eddy current density and (b) magnetic field with/without Aluminum sheet (yellow: Litz coil, light blue: ferrite cores, and pink: Aluminum sheet).

It has the advantages of simple structure, easy to analyze and high precision. The model consists of equivalent series resistance R_s, equivalent parallel resistance R_{cp} that can be ignored, and ideal capacitance C. I_{co} and T are the charging current and time span from 0 to t_1, respectively, U_{ci} and $U_{\mathrm{co}}(t_i)$ are the initial capacitor voltage and terminal or charging voltage at time t_i, respectively. The parameters of the supercapacitor used in this system are listed in Table III [47].

When the charging current I_{co} is constant, based on the KVL circuit theory, the supercapacitor terminal voltage $U_{\mathrm{co}}(t_i)$ can be expressed as

$$U_{\mathrm{co}}\left(t_i\right) = I_{\mathrm{co}} R_s + U_{\mathrm{ci}}. \tag{22}$$

During the time span from 0 to t_1, the variation of supercapacitor terminal voltage $U_{\mathrm{co}}(t_i)$ is $U_{\mathrm{c}\Delta}$, and the equations of $U_{\mathrm{co}}(t_{\mathrm{i}})$ and charging current I_{co} are shown as

$$\begin{cases} U_{\mathrm{co}}\left(t_1\right) = I_{\mathrm{co}} R_s + U_{c1} \\ I_{\mathrm{co}} = C\dfrac{dU_{c\Delta}}{dt} = C\dfrac{\left(U_{c1} - U_{c0}\right)}{T} \end{cases}. \tag{23}$$

Then, the equivalent load resistance R_{cL} of the supercapacitor at time t_1 can be deduced as

$$R_{\mathrm{cL}} = \frac{U_{\mathrm{co}}(t_1)}{I_{\mathrm{co}}} = \left(R_s + \frac{U_{c0}}{I_{\mathrm{co}}}\right) + \frac{T}{C}. \tag{24}$$

According to (24) and Table III, when the supercapacitor is charged from 10 to 92 V, equivalent load resistance as a function

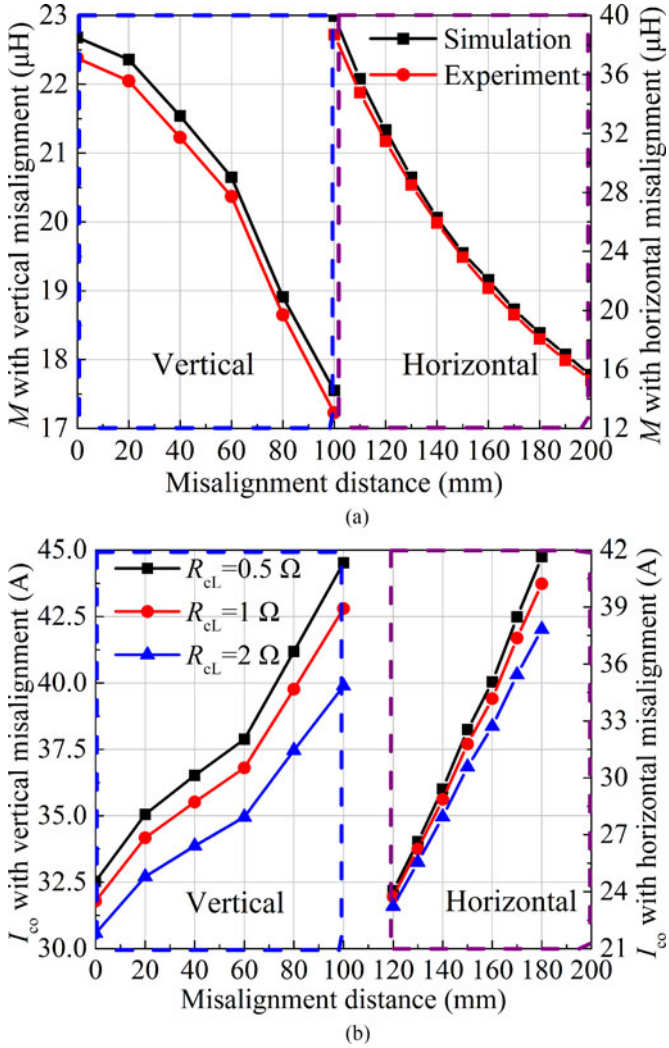

Fig. 10. Misalignment with (a) mutual inductance M and (b) charging current $I_{\rm co}$.

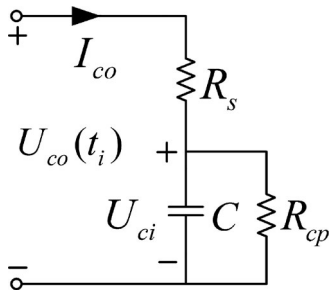

Fig. 11. Equivalent circuit model of supercapacitor.

of the charging current and charging time is experimentally verified, and the results are plotted in Fig. 12.

It shows that when the charging current is constant, equivalent load resistance $R_{\rm cL}$ has a linear relationship with the charging time. Under the same charging time, the larger the charging current is, the smaller the corresponding $R_{\rm cL}$ is. Hence, it further proves that the supercapacitor powered WPT system features a variable load whose equivalent load resistance has the characteristic of dynamically changing and small value range. It

TABLE III
PARAMETERS OF SUPERCAPACITOR MODULES

Symbol	Quantity	Value
C (F)	Rated capacitance	82.5
$R_s\,(\Omega)$	Equivalent series resistance	0.014
$R_{\rm cp}\,(\Omega)$	Equivalent parallel resistance	10 000
$U_{\rm comax}$ (V)	Maximum voltage	92
U_o (V)	Initial voltage	10
N	Number of series connected modules	2

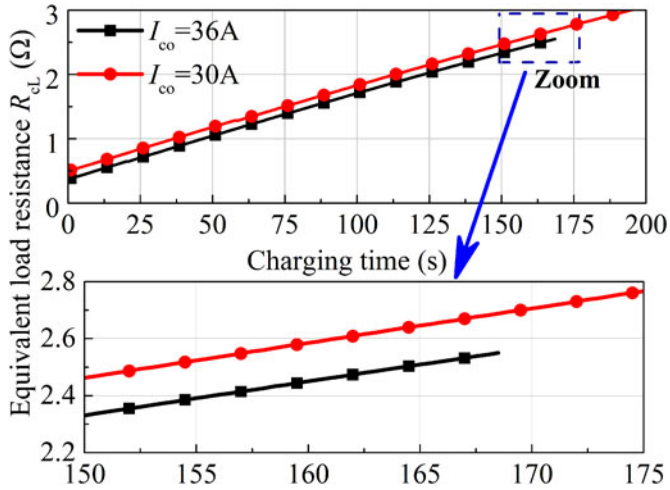

Fig. 12. Equivalent load resistance versus charging time.

should be noted that the maximum voltage of the supercapacitor modules are set to be 92 V (not 96 V stated in the datasheet [47]), with the consideration of the voltage unbalance between the supercapacitor modules and limited precision of the voltage sensor and controller [48].

B. Practical Secondary Controller Implementation

To practically realize the charging current regulation in this WPT system, secondary side control based Buck converter is implemented, as shown in Fig. 13(a). The duty cycle of the Buck converter's driving pulse-width-modulation (PWM) signal is used as the control variable to maintain the charging current constant. Two sensors are necessary for the WPT system: one is a current sensor that is used to measure the charging current, and then send the current signal to the Buck converter's controller; the other is a voltage sensor that is used to monitor the supercapacitor terminal voltage to decide the start or stop charging signal. In order to design the PI controller, the state space equations are deduced firstly, so as to obtain the transfer function of the charging current [49].

As shown in Fig. 13(a), $R_{\rm on-ds}$ is the conductive resistance of IGBT and diode $D_{\rm B}$, $R_{\rm L}$ is the internal resistance of inductor $L_{\rm B}$, $i_{\rm co}$ is the charging current, and $v_{\rm in}$ and $v_{\rm co}$ are the input and output voltages of the Buck converter, respectively. The WPT system's operating frequency (85.5 kHz) is much higher than the Buck converter's switching frequency (20 kHz) and the converter operates in continuous conduction mode (CCM). To

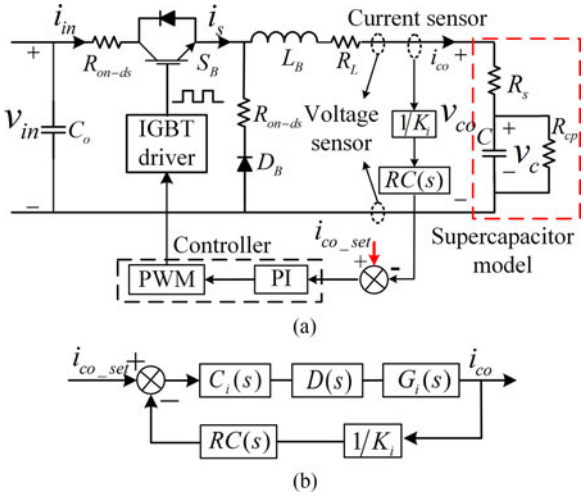

Fig. 13. Control block diagram of the Buck converter. (a) Buck converter model and (b) control block diagram.

apply the state space averaging method, a commutation function $u(t)$ is defined in the following equation first [50]:

$$u(t) = \begin{cases} 0, & 0 < t < dT_s \\ 1, & dT_s < t < T_s. \end{cases} \tag{25}$$

The above function depends on the Buck converter's driving PWM signal whose period is T_s, and then the differential equations can be expressed as follows:

$$\begin{cases} L_B \dfrac{di_{\rm co}(t)}{dt} = v_{\rm in}(t)u(t) - v_{\rm co}(t) - R' i_{\rm co}(t) \\ C \dfrac{dv_{\rm co}(t)}{dt} = i_{\rm co}(t) - \dfrac{v_{\rm co}(t)}{R_{\rm cp}} + \dfrac{R_s}{R_{\rm cp}} i_{\rm co}(t) + CR_s \dfrac{di_{\rm co}(t)}{dt} \\ i_{\rm in}(t) = i_{\rm co}(t)u(t) \end{cases} \tag{26}$$

where $R' = R_{\rm on-ds} + R_L$. According to the small signal model, the state space equations in one period T_s is expressed as

$$\begin{cases} L_B \dfrac{d\langle i_{\rm co}(t)\rangle_{T_s}}{dt} + R' \langle i_{\rm co}(t)\rangle_{T_s} = d\langle v_{\rm in}(t)\rangle_{T_s} - \langle v_{\rm co}(t)\rangle_{T_s} \\ C \dfrac{d\langle v_{\rm co}(t)\rangle_{T_s}}{dt} = \langle i_{\rm co}(t)\rangle_{T_s} - \dfrac{\langle v_{\rm co}(t)\rangle_{T_s}}{R_{\rm cp}} + \dfrac{R_s}{R_{\rm cp}} \langle i_{\rm co}(t)\rangle_{T_s} \\ \qquad + CR_s \dfrac{d\langle i_{\rm co}(t)\rangle_{T_s}}{dt} \langle i_{\rm in}(t)\rangle_{T_s} = d\langle i_{\rm co}(t)\rangle_{T_s} \end{cases} \tag{27}$$

where $\langle i_{\rm co}(t)\rangle_{T_s}$, $\langle i_{\rm in}(t)\rangle_{T_s}$, $\langle v_{\rm co}(t)\rangle_{T_s}$ and $\langle v_{\rm in}(t)\rangle_{T_s}$ are the average values of $i_{\rm co}$, $i_{\rm in}$, $v_{\rm co}$, and $v_{\rm in}$, respectively, and d is the duty cycle. Suppose that the above variables' equilibrium points are $I_{\rm co}$, $I_{\rm in}$, $V_{\rm co}$, $V_{\rm in}$, and D, respectively. Then, the equations of the small signal model can be further deduced as

$$\begin{cases} L_B \dfrac{d\hat{i}_{\rm co}(t)}{dt} + R' \hat{i}_{\rm co}(t) = [D\hat{v}_{\rm in}(t) + d\hat{v}_{\rm in}(t) + \hat{d}\, v_{\rm in}(t)] - \hat{v}_{\rm co}(t) \\ C \dfrac{d\hat{v}_{\rm co}(t)}{dt} - CR_s \dfrac{d\hat{i}_{\rm co}(t)}{dt} = \left(1 + \dfrac{R_s}{R_{\rm cp}}\right) \hat{i}_{\rm co}(t) - \dfrac{\hat{v}_{\rm co}(t)}{R_{\rm cp}}. \end{cases} \tag{28}$$

Furthermore, ignore the two order perturbation and implement the Laplace transformation on (26), the following

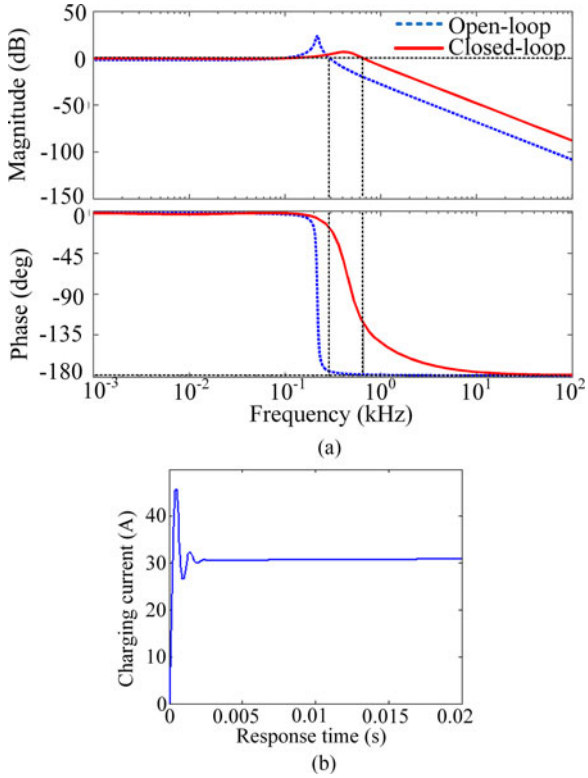

Fig. 14. Bode diagram of the open-loop and closed-loop control schemes. (a) Bode diagram and (b) charging current.

equations can be derived:

$$\begin{cases} (L_B s + R_{\rm on-ds} + R_L)\, \hat{i}_{\rm co}(s) = D\, \hat{v}_{\rm in}(s) + V_1\, \hat{d}(s) - \hat{v}_{\rm co}(s) \\ (R_{\rm cp} C s + 1)\, \hat{v}_{\rm co}(s) = (R_{\rm cp} R_s C s + R_{\rm cp} + R_s)\, \hat{i}_{\rm co}(s). \end{cases} \tag{29}$$

Considering that the equivalent parallel resistance $R_{\rm cp}$ in the supercapacitor is large enough. Combined with (29) and assume that $\hat{v}_{\rm in}(s) = 0$, the open-loop transfer function of the charging current is

$$G_i(s) = \frac{\hat{i}_{\rm co}(s)}{\hat{d}(s)} = \frac{V_1 C s}{CLs^2 + (R_{\rm on-ds}C + R_L C + R_s C)s + 1}. \tag{30}$$

As shown in Fig. 13(b), the closed-loop control block diagram that is applied to realize the constant charging current mainly consists of the transfer functions of PI controller $C_i(s)$, controller delay $D(s)$, filter $RC(s)$ and current sensor's sampling proportional coefficient $1/K_i$. Through the pole placement method, the closed-loop transfer function of the charging current is

$$G_{\rm i-closed}(s) = \frac{\left(k_p + \frac{k_i}{s}\right) e^{-Ts} G_i(s)}{1 + \frac{1}{K_1}\left(k_p + \frac{k_i}{s}\right) e^{-Ts} G_i(s) \left(1 + \frac{s}{2\pi f}\right)^{-2}}. \tag{31}$$

As shown in Fig. 14(a), the Bode diagram of the open-loop and closed-loop control schemes is analyzed by MATLAB Simulink software, and their corresponding phase margins are 3.43° and 57.4°, respectively. Compared with the open-loop

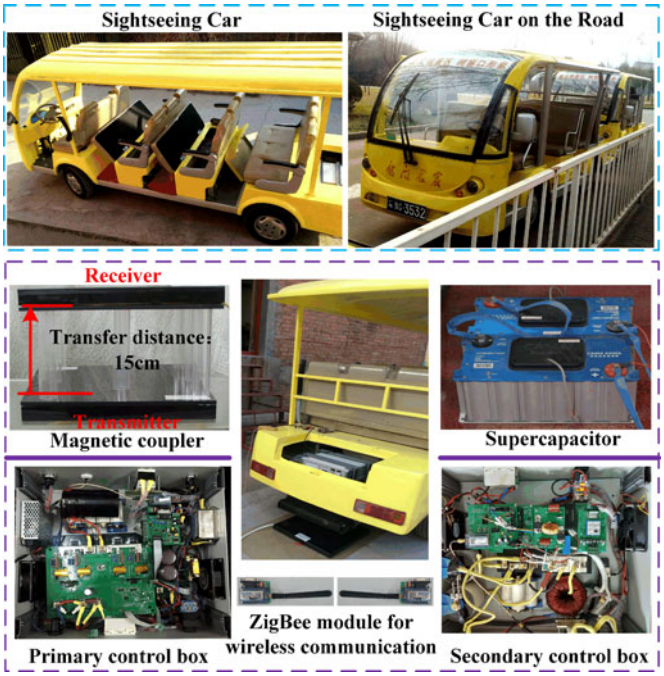

Fig. 15. Experimental setup of the WPT system.

TABLE IV
PARAMETERS OF THE EXPERIMENTAL SYSTEM

Symbol	Quantity	Value
L_1	Primary side coil inductance	$160.1\ \mu$H
C_1	Primary side resonant capacitance	21898.33 pF
A_1	Primary side transmitter size	40 cm $*$ 40 cm
L_2	Secondary side coil inductance	$79.5\ \mu$H
C_2	Secondary side resonant capacitance	43585.39 pF
A_2	Secondary side transmitter size	40 cm $*$ 40 cm
u_i (23 °C)	Initial permeability	3200
B_s (25 °C)	Saturated permeability	520 mT
D	Transfer distance	15 cm
f_s	Operating frequency	85.5 kHz
$U_{\rm in}$	System input voltage	310 dc
$\rm I_{co}$	Charging current	31.5 A
W	Whole system weight	35 kg

operation, it is obvious that the closed-loop control stability of the Buck converter is ensured. Then, combined with the designed PI controller, the charging current versus response time is also obtained by simulation, as shown in Fig. 14(b).

V. EXPERIMENTAL VALIDATION

To demonstrate the proposed 3-kW WPT system and design procedure, an experimental setup that features constant current charging for supercapacitor is built and installed in the sightseeing car, as shown in Fig. 15. The parameters of designed system are tabulated in Table IV.

A. Experimental System on the Sightseeing Car

As shown in Fig. 15, the experimental setup mainly consists of the primary and secondary side control box, magnetic coupler and supercapacitor (system load). The VSI topology H-bridge inverter in the primary side control box works at 85.5 kHz with a fixed frequency, and generates an ac magnetic flux in the transmitter. The buck converter in the secondary side control box is controlled by the PWM signal (20 kHz) whose duty cycle is adjustable. Two 2.4-GHz ZigBee wireless communication modules are used to exchange system operating state signal (the signal of start or stop charging, over current protection and so on, but not for power transfer adjustment) between the primary and secondary sides. The coils in the magnetic coupler are made of the Litz wire of 0.12 mm/1000 strands with a diameter of 4.3 mm. The rectangular structure of the coils is carefully designed to lower the ac resistance. In addition, both of the ferrite core and Aluminum sheet are optimized to enhance the mutual inductance and magnetic shielding, as mentioned in Section III.

The WPT system's charging process consists of the following stages: car detecting, start charging, and stop charging.

1) *Car detecting stage:* High sensitivity three axis magnetic sensor in the receiver and magnetic marker (permanent magnet) in the transmitter are applied. When the car stops above the transmitter, the magnetic sensor detects the magnetic field generated by the magnetic marker, a feedback signal is sent to the driver in the car, and the system is ready to be turned-on by the driver.
2) *Start charging stage:* After the car is detected, the driver pushed the "start charging button." The secondary side is powered, the Buck converter and control circuit are firstly activated. Through the wireless communication, the start charging signal is sent from the secondary side controller to the primary side controller. The H-bridge inverter and control circuit are activated. Then the whole system charging process is ready, and the power is transferred to the supercapacitor wirelessly.
3) *Stop charging stage:* When the terminal voltage of the supercapacitor approaches its maximum voltage, the controller in the secondary side sends the stop charging signal to the controller in the primary side. The input power for the WPT system is cut off through the switch that controlled by the primary side controller. Then the driver pushes the "stop charging button." Supercapacitor stops charging, and then the whole charging process is completed.

B. Open-Loop System Operation Test

The design rationality of the Type IV magnetic coupler is verified by experiments. Assume that the Buck converter operates in open-loop, the duty cycle D is 0.6 and the supercapacitor is set to be wirelessly charged from 10 to 70 V, two different coil turns of the Type IV magnetic coupler are fabricated and the parameters are listed in Table V.

As shown in Fig. 16, the influence of the mutual inductance on charging current and system efficiency coincides with (18) and (19). When mutual inductance M is large, although the charging current is small and the charging time is long, the system efficiency is high and decreased rate of charging current

TABLE V
PARAMETERS OF TWO DIFFERENT TYPE IV MAGNETIC COUPLERS

Parameters	Type IV (a)	Type IV (b)
N_1	10	15
L_1	81.1 μH	160.1 μH
N_2	5	9
L_2	26.2 μH	79.5 μH
M	11.2 μH	22.8 μH

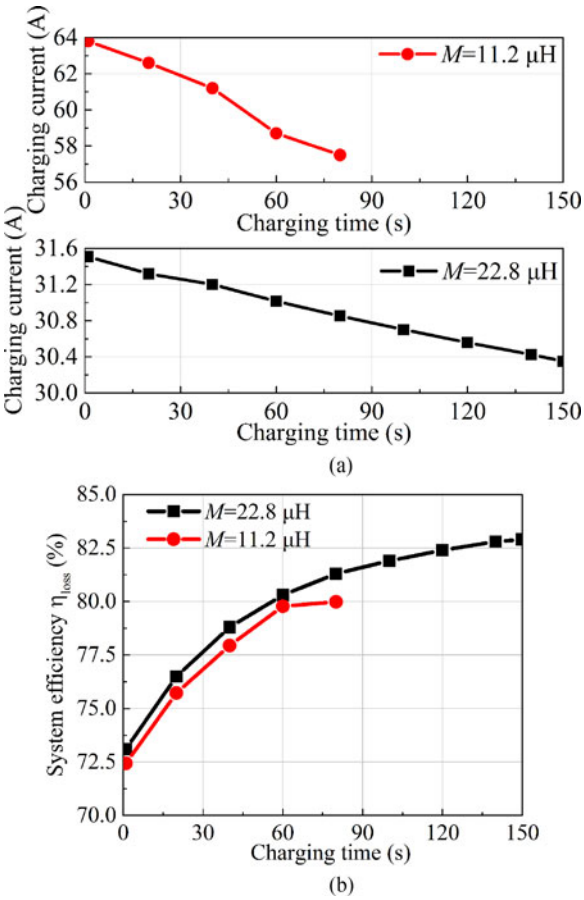

Fig. 16. Open-loop system test with mutual inductance. (a) Charging current and (b) system efficiency.

is small. To meet the system required 31.5-A charging current, the Type IV (b) magnetic coupler with $M = 22.8\,\mu$H is more suitable.

Once the Type IV (b) magnetic coupler is chosen, the system efficiency and charging current versus duty cycle are tested in open-loop. Suppose that the supercapacitor is set to be wireless charged from 10 to 92 V. From Fig. 17, it can be seen that the larger the duty cycle D is, the smaller the system efficiency and charging current are. Compared with a large duty cycle, the decreased rate of the charging current is larger for a small duty cycle. Meanwhile, due to the charging current becomes small, the charging time will increase for a complete charging process.

At the beginning of wireless charging, due to the small equivalent load resistance R_{cL}, the system efficiency is relatively low. As the charging time increases, R_{cL} becomes large and

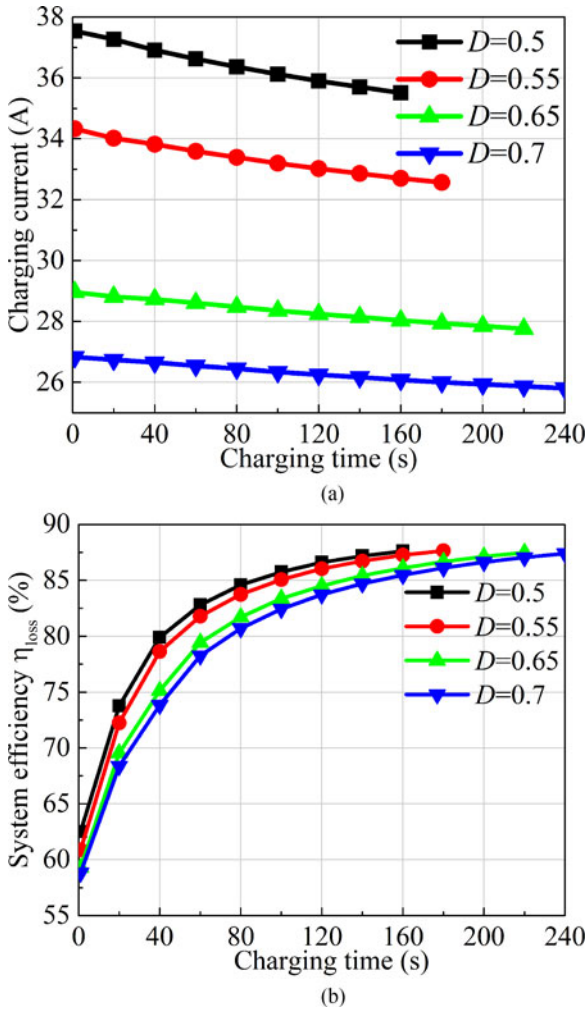

Fig. 17. Open-loop system test with duty cycle. (a) Charging current and (b) system efficiency.

approximates to the system rated load, and then the system efficiency significantly improves. Meanwhile, with the duty cycle D decreases per 0.05, the charging current increases 1–3A.

C. Validation of Secondary Side Control Scheme

In the open-loop operation test, the relationship between the charging current and duty cycle is obtained. To further validate the PI control scheme of the Buck converter, we test the closed-loop WPT system in a complete charging process of 200 s. As shown in Fig. 18, with the linear increase of the equivalent load resistance, the duty cycle that is adjusted by PI controller decreases automatically, so as to maintain the constant charging current.

It should be noted that the charging current regulation is only realized by the secondary side closed-loop control, no other control methods are implemented to adjust the input power on the primary side. Therefore, the wireless communication between the primary and secondary sides can be eliminated, and then the speed and stability can be significantly improved, which is always essential to the practical applications [6], [9].

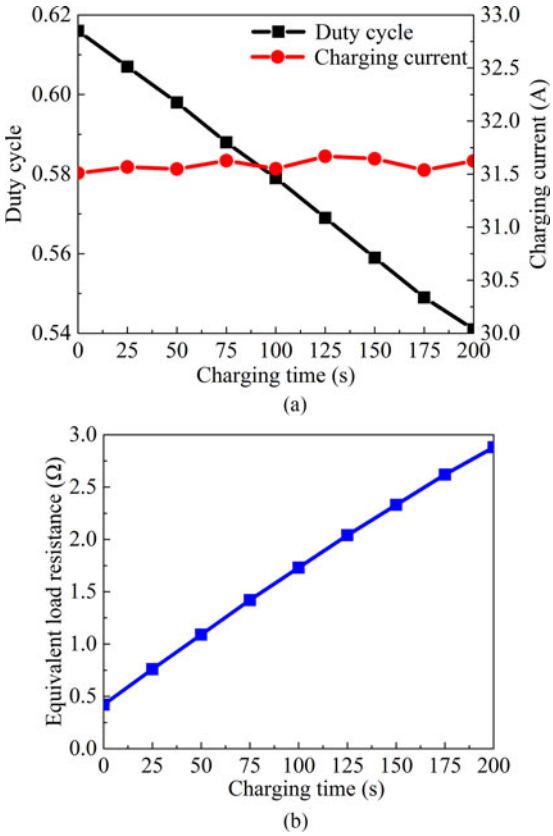

Fig. 18. Closed-loop operation by secondary side control. (a) Duty cycle adjustment and (b) equivalent load resistance.

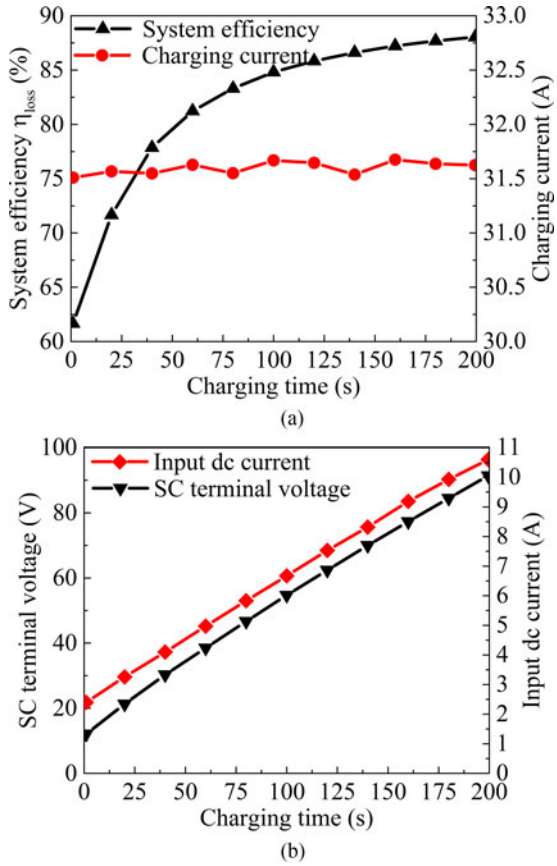

Fig. 19. Closed-loop system test. (a) Charging current and system efficiency and (b) SC terminal voltage and input dc current.

D. Closed-Loop System Operation Test

With the designed control scheme, the sightseeing car supercapacitor is charged wirelessly within the charging time of 200 s. The system efficiency and charging current versus charging time are plotted in Fig. 19.

During the complete charging process, the 31.5-A constant charging current is achieved. Due to the feedback resistance on the primary side decreases when the supercapacitor terminal voltage increases, the primary side input dc current increases to maintain the required power by the supercapacitor [9]. Meanwhile, the system efficiency maintains above 80% during the charging time of 45–200 s, which accounts for 77.5% of the whole charging process. Although the precision of charging current is limited by the current sensor and resolution of the controller, the accuracy of the system efficiency and average value of the charging current that are measured by Yokogawa Precision Power Analyzer WT1800 is less than 1%.

As shown in Fig. 20, the maximum power transfer capability of the designed WPT system is tested by a Yokogawa WT1800 Power Analyzer. When the charging current is 31.51 A, the WPT system can achieve the maximum system efficiency of 88.05% under the maximum transfer power of 2.86 kW.

During the closed-loop operation test, the operating waveforms that are measured by Tektronix Oscilloscope MSO4054B are shown in Fig. 21.

It is obvious that the transmitter current lags of the H-bridge inverter output voltage as shown in the red circle in Fig. 21,

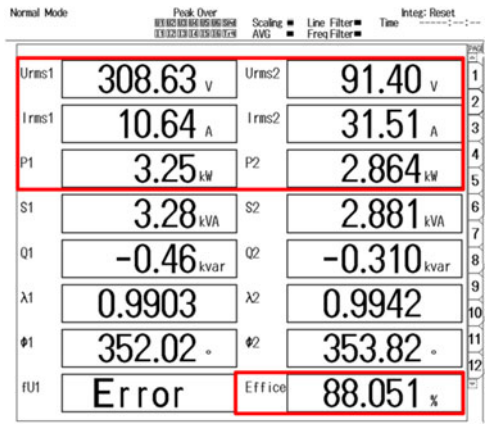

Fig. 20. Closed-loop system maximum power transfer capability test. (U_{rms1}, I_{rms1}, and P_1 are the system input dc voltage, current, and power; U_{rms2}, I_{rms2}, and P_2 are the SC terminal voltage, charging current, and transferred power; *Effice* is the system efficiency).

which means the operating frequency of the H-bridge inverter is larger than the primary side resonant frequency. Therefore, the H-bridge inverter has an inductive load to achieve ZVS, and then EMI and switching losses of MOSFETs can be further suppressed [35]. The average value of the charging current waveform in Fig. 21 is 31.5 A, which is consistent with the measurement obtained by the Yokogawa WT1800 Power Analyzer.

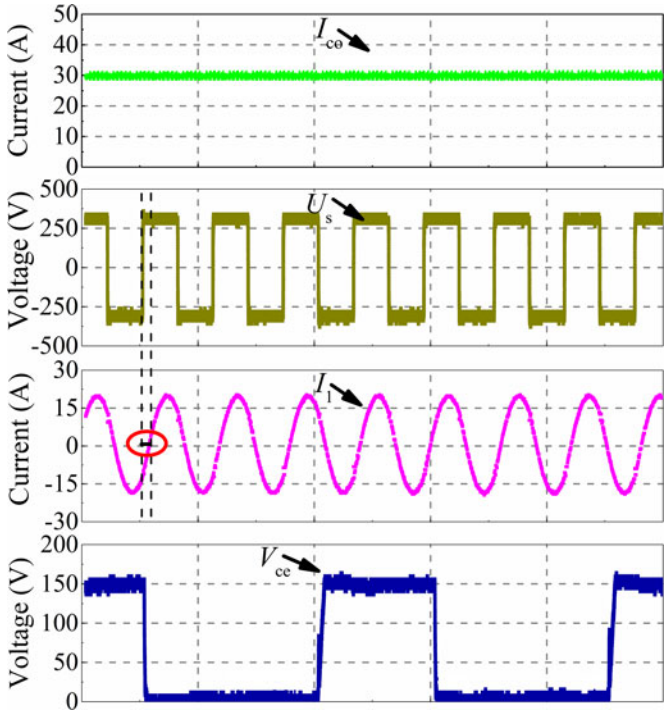

Fig. 21. Closed-loop system working waveforms. (SC's charging current $I_{\rm co}$, H-bridge inverter output voltage U_s, Transmitter current I_1, and Buck converter's IGBT voltage $V_{\rm ce}$). *X*-scale: 20 μs/division.

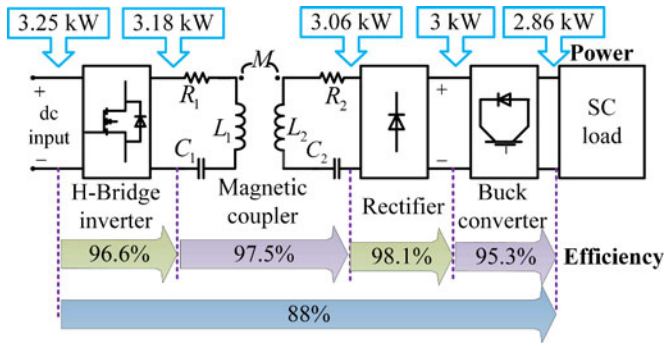

Fig. 22. System losses and efficiency analysis.

E. System Losses Analysis

In order to further improve the system efficiency, which is our future work, system losses with the transferred power of 2.86 kW are analyzed, as shown in Fig. 22. The losses mainly occur in the following parts: H-bridge inverter, magnetic coupler, secondary side rectifier, and Buck converter.

According to Figs. 19 and 22, compared with the transferred power of 500 W, when the transferred power is 2.86 kW, system efficiency is improved from 68% to 88%. The reason is that when the transferred power is low, the system operated under light load condition, the system inherent losses, such as inverter's loss, rectifier's loss, and so on, accounting for a large part of the system's input power. However, when the transferred power is high, the inherent losses account for the input power decrease, and then system efficiency will be significantly improved [51].

VI. Conclusion

This paper outlines the overall design and implementation of a practical 3-kW WPT system for supercapacitor charge. The designed system is able to achieve 31.5 A constant current charging with the maximum 88.05% system efficiency across a transfer distance of 15 cm. In addition, the proposed and optimized magnetic coupler is able to significantly reduce the weight, and cost, and enhances magnetic shielding without compromising system performance. Then, the closed-loop control of the Buck converter with PI controller are designed to realize the charging current regulation for the supercapacitor whose equivalent load resistance changing linearly versus charging time. Finally, the designed WPT system is realized in a sightseeing car and the correctness of the theoretical analysis and simulation are verified.

References

[1] S. Li, W. Li, J. Deng, T. D. Nguyen, and C. C. Mi, "A double-sided LCC compensation network and its tuning method for wireless power transfer," *IEEE Trans. Veh. Technol.*, vol. 64, no. 6, pp. 2261–2273, Jun. 2015.

[2] S. Lee, B. Choi, and C. T. Rim, "Dynamics characterization of the inductive power transfer system for online electric vehicles by Laplace phasor transform," *IEEE Trans. Power Electron.*, vol. 28, no. 12, pp. 5902–5909, Dec. 2013.

[3] M. Sato, G. Yamamoto, D. Gunji, T. Imura, and H. Fujimoto, "Development of wireless In-wheel motor using magnetic resonance coupling," *IEEE Trans. Power Electron.*, vol. 31, no. 7, pp. 5270–5278, Jul. 2016.

[4] S. Y. Choi, B. W. Gu, S. Y. Jeong, and C. T. Rim, "Advances in wireless power transfer systems for roadway-powered electric vehicles," *IEEE J. Emerg. Sel. Topics Power Electron.*, vol. 3, no. 1, pp. 18–36, Mar. 2015.

[5] N. Keeling, G. A. Covic, and J. T. Boys, "A unity-power-factor IPT pickup for high-power applications," *IEEE Trans. Ind. Electron.*, vol. 57, no. 2, pp. 744–751, Feb. 2010.

[6] H. Li, J. Li, K. Wang, W. Chen, and Y. Xu, "A maximum efficiency point tracking control scheme for wireless power transfer systems using magnetic resonant coupling," *IEEE Trans. Power Electron.*, vol. 30, no. 7, pp. 3998–4008, Jul. 2015.

[7] M. Fu, C. Ma, and X. Zhu, "A cascaded Boost-Buck converter for high efficiency wireless power transfer systems," *IEEE Trans Ind. Informat.*, vol. 10, no. 3, pp. 1972–1980, Aug. 2014.

[8] M. Mcdonough, "Integration of inductively coupled power transfer and hybrid energy storage system: A multi-port power electronics interface for battery powered electric vehicles," *IEEE Trans. Power Electron.*, vol. 30, no. 11, pp. 6423–6433, Nov. 2015.

[9] T. Hiramatsu, X. Huang, M. Kato, T. Imura, and Y. Hori, "Wireless charging power control for HESS through receiver side voltage control," in *Proc. 30th Annu. IEEE Appl. Power Electron. Conf. Expo.*, Mar. 15–19, 2015, pp. 1614–1619.

[10] A. P Hu, Y. W. You, F. B Chen, and D. McCormick, "Wireless power supply for ICP devices with hybrid supercapacitor and battery storage," *IEEE J. Emerg. Sel. Topics Power Electron.* vol. 4, no. 1, pp. 273–279, Mar. 2016.

[11] P. Aqueveque and J. Barboza, "Wireless power system for charge supercapacitors as power sources for implantable devices," in *Proc. IEEE PELS Workshop Emerg. Technol.*, 2015, pp. 1–5.

[12] J. I Itoh, K. Noguchi, and K. Orikawa, "System design of electric assisted bicycle using EDLCs and wireless charger," in *Proc. IEEE Int. Conf. Power Electron.*, 2014, pp. 2277–2284.

[13] W. Lajnef, J. M. Vinassa, O. Briat, S. Azzopardi, and E. Woirgard, "Characterization methods and modelling of ultracapacitors for use as peak power sources," *J. Power Sources.*, vol. 168, no. 2, pp. 553–560, Jun. 2007.

[14] R. German, A. Hammar, R. Lallemand, A. Sari, and P. Venet, "Novel experimental identification method for a supercapacitor multipore model in order to monitor the state of health," *IEEE Trans. Power Electron.*, vol. 31, no. 1, pp. 548–559, Jan. 2016.

[15] R. L. Spyker and R. M. Nelms, "Classical equivalent circuit parameters for a double-layer capacitor," *IEEE Trans. Aerosp. Electron. Syst.*, vol. 36, no. 3, pp. 829–836, Jul. 2000.

[16] R. Chai and Y. Zhang, "A practical supercapacitor model for power management in wireless sensor nodes," *IEEE Trans. Power Electron.*, vol. 30, no. 12, pp. 6720–6730, Dec. 2015.
[17] S. Raju, R. Wu, M. Chan, and C. P. Yue, "Modeling of mutual coupling between planar inductors in wireless power applications," *IEEE Trans. Power Electron.*, vol. 29, no. 1, pp. 481–490, Jan. 2014.
[18] M. Budhia, J. T. Boys, G. A. Covic, and C. Y. Huang, "Development of a single-sided flux magnetic coupler for electric vehicle IPT charging systems," *IEEE Trans. Ind. Electron.*, vol. 60, no. 1, pp. 318–328, Jan. 2013.
[19] D. Kurschner, C. Rathge, and U. Jumar, "Design methodology for high efficient inductive power transfer systems with high coil positioning flexibility," *IEEE Trans. Ind. Electron.*, vol. 60, no. 1, pp. 372–381, Jan. 2013.
[20] M. Budhia, G. Covic, and J. T. Boys, "Design and optimization of circular magnetic structures for lumped inductive power transfer systems," *IEEE Trans. Power Electron.*, vol. 26, no. 11, pp. 3096–3108, Nov. 2011.
[21] H. H. Wu, A. Gilchrist, K. D. Sealy, and D. Bronson, "A high efficiency 5 kW inductive charger for EVs using dual side control," *IEEE Trans. Ind. Info.*, vol. 8, no. 3, pp. 585–595, Aug. 2012.
[22] Z. Cheng, L. Yang, S. Kai, and C. Zhu, "Design and loss analysis of loosely coupled transformer for an underwater high-power inductive power transfer system," *IEEE Trans. Magn.*, vol. 51, no. 7, Jul. 2015, Art. no. 8106307.
[23] H. Kim *et al.*, "Coil design and measurements of automotive magnetic resonant wireless charging system for high-efficiency and low magnetic field leakage," *IEEE Trans. Microw. Theory Techn.*, vol. 64, no. 2, pp. 383–400, Feb. 2016.
[24] S. Kim, H.-H. Park, J. Kim, and S. Ahn, "Design and analysis of a resonant reactive shield for a wireless power electric vehicle," *IEEE Trans. Microw Theory. Techn.*, vol. 62, no. 4, pp. 1057–1066, Apr. 2014.
[25] Liu, N., Habetler, T. G., "Design of a universal inductive charger for multiple electric vehicle models," *IEEE Trans. Power Electron.*, vol. 30, no. 11, pp. 6378–6390, Nov. 2015.
[26] D. Ahn and S. Hong, "Wireless power transmission with self-regulated output voltage for biomedical implant," *IEEE Trans. Ind. Electron.*, vol. 61, no. 5, pp. 2225–2235, May 2014.
[27] K. E. Koh, T. C. Beh, T. Imura, and Y Hori, "Impedance matching and power division using impedance inverter for wireless power transfer via magnetic resonant coupling," *IEEE Trans. Ind. Electron.*, vol. 50, no. 3, pp. 2061–2070, May 2014.
[28] J. Kim, D. Kim, Y. Park, "Analysis of capacitive impedance matching networks for simultaneous wireless power transfer to multiple devices," *IEEE Trans. Ind. Electron.*, vol. 62, no. 5, pp. 2807–2813, May 2015.
[29] H. Ishihara *et al.*, "A voltage ratio-based efficiency control method for 3 kW wireless power transmission," in *Proc. IEEE Appl. Power Electron. Conf. Expo.*, 2014, pp. 1312–1316.
[30] M. Fu, H. Yin, X. Zhu, and C. Ma, "Analysis and tracking of optimal load in wireless power transfer systems," *IEEE Trans. Power Electron.*, vol. 30, no. 7, pp. 3952–3963, Jul. 2015.
[31] A. Berger, M. Agostinelli, S. Vesti, and A. Oliver, "A wireless charging system applying phase-shift and amplitude control to maximize efficiency and extracted power," *IEEE Trans. Power Electron.*, vol. 30, no. 11, pp. 6338–6348, Nov. 2015.
[32] T. Diekhans and R. W. De, "A dual-side controlled inductive power transfer system optimized for large coupling factor variations and partial Load," *IEEE Trans. Power Electron.*, vol. 30, no. 11, pp. 6320–6328, Nov. 2015.
[33] J. Zhang *et al.*, "Magnetic coupling resonance type wireless energy transmission device based on panel magnetic core," C. N. Patent 1 026 112 09A, Jul. 25, 2012.
[34] S. Anand, S. K. Gundlapalli, and B. G. Femandes, "Transformer-less grid feeding current source inverter for solar photovoltaic system," *IEEE Trans. Ind. Electron.*, vol. 61, no. 10, pp. 5334–5344, Oct. 2014.
[35] Y. Zhang, K. Chen, F. He, Z. Zhao, T. Liu, and L. Yuan, "Closed-form oriented modeling and analysis of wireless power transfer system with constant-voltage source and load," *IEEE Trans. Power Electron.*, vol. 31, no. 5, pp. 3472–3481, May 2016.
[36] T. Kerekes, R. Teodorescu, P. Rodríguez, G. Vázquez, and E. Aldabas, "A new high-efficiency single-phase transformer-less PV inverter topology," *IEEE Trans. Ind. Electron.*, vol. 58, no. 1, pp. 184–191, Jan. 2011.
[37] J. Sallan, J. L. Villa, A. Llombart, and J. F. Sanz, "Optimum design of ICPT systems applied to electric vehicle battery charge," *IEEE Trans. Ind. Electron.*, vol. 56, no. 6, pp. 2140–2149, Jun. 2009.
[38] H. Cai, L. Shi, and Y. Li, "Harmonic-based phase-shifted control of inductively coupled power transfer," *IEEE Trans. Power Electron.*, vol. 29, no. 4, pp. 594–602, Feb. 2014.
[39] S. Y. Jeong, S. Y. Choi, M. R. Sonapreetha, and C. T Rim, "DQ-quadrature power supply coil sets with large tolerances for wireless stationary EV chargers," in *Proc. IEEE PELS Workshop Emerg. Technol.*, 2015, pp. 1–6.
[40] N. Hasan, H. Wang, T. Saha, and Z. Pantic, "A novel position sensorless power transfer control of lumped coil-based in-motion wireless power transfer systems," in *Proc. IEEE Energy Convers. Congr. Expo.*, 2015, pp. 586–593.
[41] S. Chen, C. Liao, and L. Wang, "Research on positioning technique of wireless power transfer system for electric vehicles," in *Proc. IEEE Transp. Electrification Asia-Pacific Conf. Expo.*, 2014, pp. 1–4.
[42] R. Beiranvand, R. Zolghadri, B. Rashidian, and H. Alavi, "Optimizing the LLC–LC resonant converter topology for wide-output-voltage and wide-output-load applications," *IEEE Trans. Power Electron.*, vol. 26, no. 11, pp. 3192–3204, Nov. 2011.
[43] L. Steigerwald, "A comparison of half-bridge resonant converter topologies," *IEEE Trans. Power Electron.*, vol. 3, no. 2, pp. 174–182, Apr. 1988.
[44] X. Nguyen *et al.*, "An efficiency optimization scheme for bidirectional inductive power transfer systems," *IEEE Trans. Power Electron.*, vol. 30, no. 11, pp. 6310–6319, Nov. 2015.
[45] W. X. Zhong and S. Y. R. Hui, "Maximum energy efficiency tracking for wireless power transfer systems," *IEEE Trans. Power Electron.*, vol. 30, no. 7, pp. 4025–4034, Jul. 2015.
[46] S. Li and C. C. Mi, "Wireless power transfer for electric vehicle applications," *IEEE J. Emerg. Sel. Topics Power Electron.*, vol. 3, no. 1, pp. 4–17, Mar. 2015.
[47] CAMA, Supercapacitor module, UCM48V165F datasheet. [Online]. Available: http://www.kmjhcama.com/show.asp?id=541
[48] D. Linzen, S. Buller, E. Karden, and R. W. D. Doncker, "Analysis and evaluation of charge-balancing circuits on performance, reliability, lifetime of supercapacitor systems," *IEEE Trans. Ind. Appl.*, vol. 41, no. 5, pp. 1135–1141, Sep./Oct. 2005.
[49] A. Emadi, "Modeling and analysis of multiconverter DC power electronic systems using the generalized state-space averaging method," *IEEE Trans. Ind. Electron.*, vol. 51, no. 3, pp. 6610–668, Jun. 2004.
[50] J. Mahdavo, A. Emaadi, D. Bellar, and M. Ehsani, "Analysis of power electronic converters using the generalized state-space averaging approach," *IEEE Trans. Circuits Syst. I, Fundam. Theory Appl.*, vol. 44, no. 8, pp. 767–770, Aug. 1997.
[51] L. Chen, G. Nagendra, J. T. Boys, and G. A. Covic, "Double-coupled systems for IPT roadway applications," *IEEE J. Emerg. Sel. Topics Power Electron.*, vol. 3, no. 1, pp. 37–49, Mar. 2015.

Zhenjie Li received the B.S. degree in measurement and control technology and communication engineering from Harbin University of Science and Technology, Harbin, China, in 2012, and the M.S. degree in electrical engineering and automation from Harbin Institute of Technology, Harbin, China, in 2014, where he is currently working toward the Ph.D. degree.

His research interests include wireless power transfer for supercapacitor and battery powered electric vehicles.

Chunbo Zhu (M'05) received the B.S. and M.S. degrees in electrical engineering and the Ph.D. degree in mechanical engineering from Harbin Institute of Technology (HIT), Harbin, China, in 1987, 1992, and 2001, respectively.

From 2003 to 2004, he was a Postdoctoral Research Fellow at PEI Research Center, National University of Ireland, Galway, Ireland. Since 1987, he has been a Lecturer at the Department of Automation Measurement and Control, HIT. He is currently a Full Professor with HIT, where he leads the Laboratory of Wireless Power Transfer and Battery Management Technologies. His current research interests include energy management systems, electric and hybrid electric vehicles, and wireless power transfer technologies.

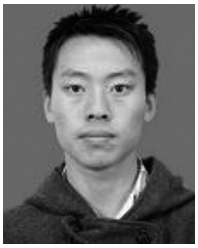

Jinhai Jiang received the B.S. degree in electronic science and the M.S. degree in electrical engineering and information, both from Northeast Petroleum University, Daqing, China, in 2010 and 2013, respectively. He is currently working toward the Ph.D. degree at Harbin Institute of Technology.

His research interests include wireless power transfer for supercapacitor and battery powered online electric vehicles.

Kai Song (M'12) received the B.S., M.S., and Ph.D. degrees in instrument science and technology from the Harbin Institute of Technology (HIT), Harbin, China, in 2005, 2007, and 2011, respectively.

In 2011, he joined the School of Electrical Engineering and Automation, HIT, as a lecturer, and was a visiting scholar in electrical engineering, The University of Tokyo, Japan, from 2014 to 2015.

Since 2011, he has been a Lecturer at the School of Electrical Engineering and Automation, HIT, and a Postdoctoral Research Fellow at the State Key Laboratory of Robotics and System, HIT, since 2013. He is currently a Visiting Scholar in electrical engineering at the University of Tokyo, Tokyo, Japan. His current research interests include wireless power transfer, wireless communication, and advanced sensor technologies.

He is currently an Associate Professor with the School of Electrical Engineering and Automation, HIT, since 2016. His current research interests concentrate in wireless power transfer, particularly in the high-power wireless power transfer system for electric vehicles and robots.

Guo Wei received the B.S. and M.S. degrees in electromagnetic measurement and instruments from Harbin Institute of Technology, China, in 1988 and 1991, respectively, and the Ph.D. degree in scientific research from Saga University, Saga, Japan, in 2003.

He is currently a Professor at the School of Electrical Engineering and Automation, Harbin Institute of Technology. His research interests include modern sensor technique, intelligent testing theory and its application, weak signal detection and processing, wireless power transfer, and near field magnetic communication.